CHEMISTRY OF MATERIALS

pubs.acs.org/cm

Article

Na^+ Preintercalated Bilayered V_2O_5 Cathode Materials for Na-Ion Batteries

Qiang Fu,* Björn Schwarz, Angelina Sarapulova, Xianlin Luo, Julian Hansen, Zhen Meng, Volodymyr Baran, Alexander Missyul, Edmund Welter, Weibo Hua, Michael Knapp, Helmut Ehrenberg, and Sonia Dsoke

Cite This: *Chem. Mater.* 2024, 36, 10176−10185

Read Online

ACCESS | Metrics & More | Article Recommendations | Supporting Information

ABSTRACT: Na^+ preintercalated bilayered vanadium oxide (NVOnH) with a large interlayer spacing of ∼11.1 Å is synthesized via a hydrothermal method. As proven by mass spectrometry and magnetization measurements, NVOnH is "oxygen-rich". NVOnH undergoes notable structural evolution and thermal instability during heating due to crystal water and O_2 release and decomposition. NVOnH and dehydrated NVOnH (NVO) deliver capacities of over 250 and 220 mAh g^{-1}, respectively, despite their fast capacity decay in the first 20 cycles and low capacity retention after 100 cycles. Moreover, the reaction mechanism and reversibility of NVOnH and NVO during Na^+-ion (de)insertion are investigated via *in operando* techniques. NVOnH experiences a two-phase and solid-solution reaction during discharge and charge processes, while NVO undergoes a different phase evolution (NVO starting with charging: two-phase reaction for the first charging and only solid solution for the following cycle; NVO starting with discharging: only a solid-solution reaction). *In operando* X-ray absorption spectroscopy demonstrates the variation of the oxidation state and the local structural environment of the V ion during Na^+ (de)insertion.

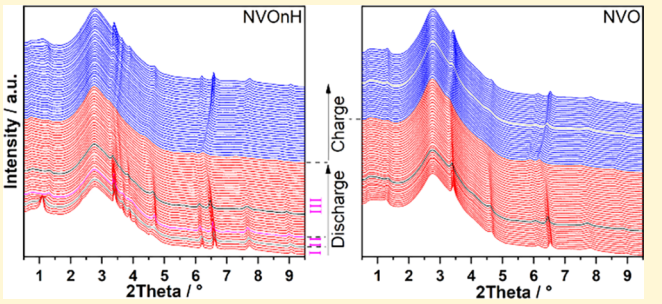

1. INTRODUCTION

Recently, Na-ion batteries (SIBs) have received much attention because of their low cost and abundant resources, and they share a similar "rocking chair principle" as Li-ion batteries (LIBs). Meanwhile, Al can be used as the current collector in both cathodes and anodes for SIBs, whereas an expensive and heavier Cu foil must be used as the current collector in anodes for LIBs because of the Li−Al alloy formation at low potentials.[1,2] Therefore, SIBs are now considered as promising candidates to meet the demand for large-scale energy storage systems and are investigated in the German cluster of excellence POLiS between the Karlsruhe Institute of Technology (KIT) and Ulm University. Currently, a variety of cathode materials including polyanionic compounds,[3,4] Prussian blue analogues,[5,6] transition metal oxides,[7−9] and organic-based materials[10,11] have been under investigation. Recently, Contemporary Amperex Technology Co., Limited (CATL) has launched commercial SIBs consisting of a Prussian white cathode and porous structure hard carbon anode, where the battery provides a high energy density of 160 Wh kg^{-1} and fast charge to 80% state of charge in 15 min.[12] Despite this progress and the potential advantages of SIBs, most of the cathode materials face structural degradation, low capacity, and slow kinetic diffusion properties during electrochemical cycling owing to the large size of Na^+ ions (1.02 Å for Na^+ vs 0.76 Å for Li^+).[13] Hence, it is essential to explore and develop high-performance cathode materials for SIBs. Moreover, the structural degradation could be improved to some extent by using nanomaterials or open tunnel structures or by employing layered materials as cathode electrodes.

Bilayered vanadium oxide ($V_2O_5{\cdot}nH_2O$) is considered as a promising high-capacity cathode material for Li-ion, Na-ion, and Mg-ion batteries[14−17] because of its large interlayer space and multivalent redox capability. Each layer consists of double-stacked ribbons of VO_6 octahedra. The V−O layers are bound by van der Waals forces, and the interlayer region is stabilized by crystallization water.[18] In addition, ion stabilization, preintercalation in the interlayer space, is regarded as an effective approach to improve the structural stability of layered transition metal oxides during electrochemical cycling. Preintercalated ions are believed to form bonds with the oxygen atoms in transition-metal−oxygen layers to act as

Received: June 27, 2024
Revised: August 18, 2024
Accepted: August 19, 2024
Published: October 14, 2024

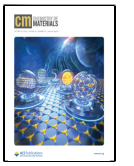

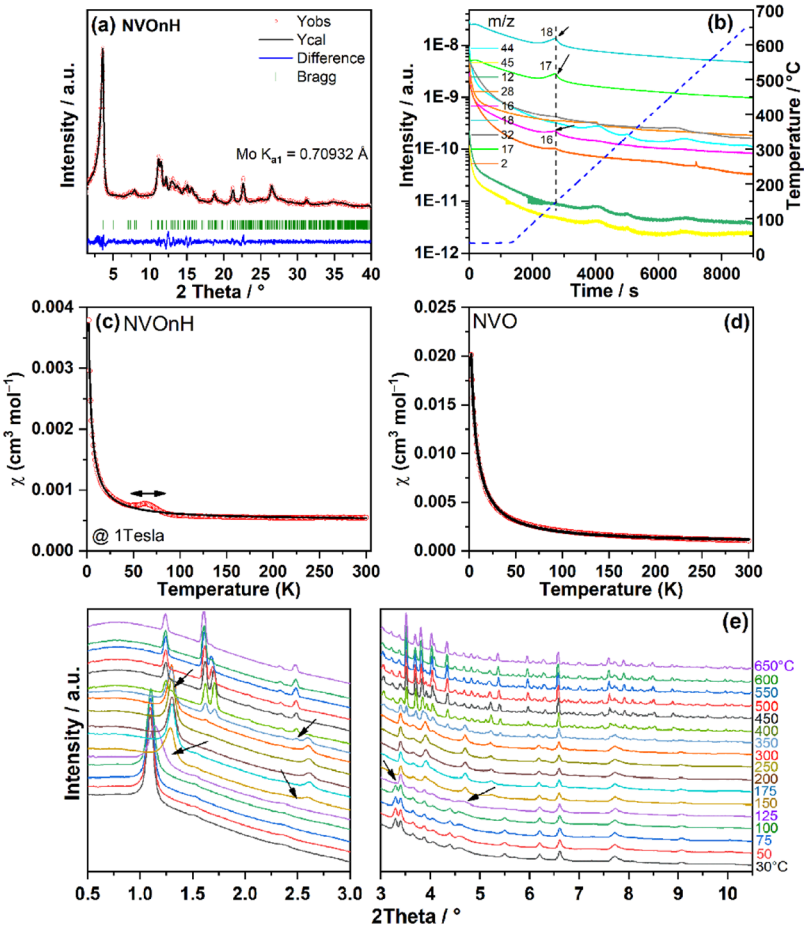

Figure 1. XRD of NVOnH nanowires (Mo $K_{\alpha 1}$, λ = 0.70932 Å) (a), TGA-MS of m/z signals (b) of NVOnH under an Ar atmosphere, magnetic susceptibility vs temperature measured at 1 T together with Curie−Weiss fit for NVOnH (c) and NVO (d), and *in situ* high-temperature synchrotron diffraction patterns (λ = 0.20732 Å, 60 keV) of NVOnH during heating from 30 to 650 °C (e).

"pillars". For example, Clites and Pomerantseva[19] prepared bilayered $M_xV_2O_5$ (M = Li, Na, K, Mg, and Ca) and demonstrated that the cyclability and rate performance of the bilayered $M_xV_2O_5$ improve with increasing interlayer spacing (9.6−13.4 Å) in LIBs. However, only a few works have focused on the study of preintercalated bilayered V_2O_5 for SIBs.[20−23] For instance, Wei et al.[20] reported that iron preintercalated vanadium oxide in SIBs shows a discharge capacity of 184 mAh g^{-1} at a current density of 0.1 A g^{-1} between 1.0 and 4.0 V vs Na^+/Na. The bilayered $Na_xV_2O_5$ prepared by Clites et al.[21] delivers a high initial discharge capacity of 365 mAh g^{-1} at 20 mA g^{-1} in 1.0−4.3 V vs Na^+/Na and a discharge capacity of 179 mAh g^{-1} after 30 cycles in SIBs. Zhao et al.[22] studied a $Na_xV_2O_5{\cdot}nH_2O$/ketjen black nanocomposite, exhibiting a discharge capacity of 239 mA h g^{-1} at 20 mA g^{-1}. Up to now, the actual reaction mechanism of Na-ion preintercalated bilayered V_2O_5 during the electrochemical processes is also still missing and the role of crystal water in the bilayered $Na_xV_2O_5$ remains unclear.

Herein, oxygen-rich Na^+ preintercalated bilayered vanadium oxide (NVOnH) nanowires with a large interplanar spacing of ∼11.1 Å were synthesized via the hydrothermal method. The physical properties, thermal stability, and phase evolution of NVOnH are first investigated. Then, the electrochemical performance of the NVOnH cathode and dehydrated NVOnH (NVO) in SIBs is studied and compared. Furthermore, the reaction mechanism of NVOnH and NVO during sodium intercalation/deintercalation in SIBs is carefully revealed using *in operando* synchrotron diffraction and X-ray absorption spectroscopy (XAS). This work provides a deep understanding of the Na^+ storage mechanism of bilayered vanadium oxide cathode materials.

2. RESULTS AND DISCUSSION

2.1. Physical Properties of NVOnH. Powder X-ray diffraction (XRD) was carried out to investigate the phase purity and structure of the synthesized vanadium oxide NVOnH. The XRD pattern shown in Figure 1a cannot be indexed according to any known structure type reported in the literature, including a known compound $Na_xV_2O_5{\cdot}nH_2O$, which consists of δ-type V_2O_5 layer stacking along the c axis and with hydrated Na^+ ions in between interlayers.[24−26] NVOnH shows a similar XRD pattern to electrolytic vanadium oxide (e-V_2O_5)[27] and e-$M_xV_2O_{5+y}{\cdot}nH_2O$,[28] demonstrating the features of a xerogel structure, where it is composed of double-layered VO_6 octahedra and VO_5 pyramids with water molecules and metal cations residing between the interlayers. NVOnH has a strong and sharp reflection at 2θ = ∼3.7° (Mo $K_{\alpha 1}$, λ = 0.70932 Å), representing an interlayer spacing of ∼11.1 Å (Figure 1a). This value is much larger than those of $Zn_{0.25}V_2O_5{\cdot}nH_2O$ (∼10.2 Å),[29] ζ-V_2O_5 (∼9.5 Å),[30] and $NH_4V_4O_{10}$ (9.8 Å)[31] and close to those of $V_2O_5{\cdot}0.5H_2O$ (10.8 Å)[32] and $NH_4V_4O_{10}{\cdot}nH_2O$ (10.9 Å).[33] The large spacing of NVOnH offers more space for Na^+ storage and facilitates

https://doi.org/10.1021/acs.chemmater.4c01739
Chem. Mater. 2024, 36, 10176−10185

Na^+-ion diffusion. Le Bail fitting demonstrates that the XRD patterns of the NVOnH material can be described by an orthorhombic structure with a *Pmmn* space group with lattice parameters of a = 11.548(2) Å, b = 3.657(1) Å, and c = 11.077(2) Å, which has a similar $a-b$ plane to V_2O_5 (a = 11.510 Å, b = 3.563 Å, and *Pmmn*).[34] Scanning electron microscopy (SEM) demonstrates a nanowire morphology with typical lengths of 300 nm to 2 μm and width of ∼50 nm (Figure S1). Furthermore, thermogravimetric analysis (TGA), X-ray photoelectron spectroscopy (XPS), and inductively coupled plasma optical emission spectroscopy (ICP-OES) were conducted to estimate the amount of crystal water and the chemical formula of NVOnH. In the TGA curve (Figure S2a), the weight loss of ∼8.7 wt % in the 100−400 °C range is attributed to crystal water and minor residual organic components. ICP-OES reveals that the ratio of Na/V in the nanowires is 0.38:2. The V 2p spectrum of the pristine NVOnH can be fitted by two doublets with V $2p_{3/2}$ at 517.4 and 516.0 eV,[35] giving an average oxidation state of $V^{4.89+}$ (Figure S2b). To maintain charge neutrality, more oxygen should exist in the material, and thus, the chemical formula of NVOnH nanowires is determined as $Na_{0.38}V_2O_{5+\delta}{\cdot}nH_2O$ ($\delta \sim 0.1$, $n \sim 1.1$). TGA coupled with mass spectrometry (TGA-MS) was performed under an Ar flow to investigate the existence of additional oxygen. Figure 1b exhibits the observed m/z signals of 16, 17, and 18 at ∼150 °C, where m/z = 17 and 18 are related to water release and m/z = 16 is ascribed to O_2 release. Note that the observed m/z signals of 44 at ∼350 °C are attributed to CO_2 release resulting from the residual organic acetate component during synthesis.

Magnetic properties of NVOnH were investigated to gain more insights into the electronic configuration of the V ions. The ZFC and FC branches are superimposed over the complete temperature region, and therefore, only the ZFC curve will be considered further. As shown in Figure 1c, the susceptibility curve obtained from the ZFC curve exhibits a clear $1/T$-like behavior, particularly visible at temperatures below ∼50 K, displaying a typical Langevin-type paramagnetism of localized moments. From the Curie−Weiss fit to the susceptibility data of NVOnH from 2 to 300 K (Figure 1c), the Curie constant, the Weiss constant, and the temperature-independent paramagnetic contribution are estimated to be 0.0104(1) $cm^3\ K\ mol^{-1}$, −1.23(5) K, and 5.88(2) $\times 10^{-4}\ cm^3\ mol^{-1}$, respectively. Therefore, the concentrations of 1.972(1) V^{5+} (diamagnetic) and 0.028(1) V^{4+} (paramagnetic with $\sqrt{3} \approx 1.73\ \mu B$ per ion) are determined, with only a small portion of V^{4+} in the NVOnH material and a correspondingly very weak paramagnetic signal only. With the assumption that 0.38 Na^+ is present next to the above-mentioned amounts of V^{5+} and V^{4+}, the demand of charge neutrality indicates an oxygen excess of $\delta_{mag} \sim 0.18$ in the NVOnH structure that is in accordance with the chemical analysis and TGA-MS results. Moreover, a small bump in the susceptibility curve between ∼50 and ∼80 K (indicated by a double-arrow in the figure) is supposed to be related to a spin glass-like behavior, as outlined below. Field scan at 2 K shows a typical behavior of Langevin-type localized moments with indications of saturation at high fields (Figure S3a). The ordered moment at 2 K and 7 T is ∼0.028 μB, which exactly matches with the concentration of V^{4+} as determined from the Curie−Weiss fit and the fact that each V^{4+} would contribute with a z-component of the magnetic moment of 1 μ_B to the measured magnetization (z is the quantization axis as defined by the direction of the external magnetic field). Interestingly, the hysteresis loops between ∼50 and ∼80 K are not closed (Figure S3b) due to time-dependent relaxation processes, specifically a spin-glass like behavior (note the slow evolving magnetization in this temperature region over time as shown in Figure S3c). The temperature cycling experiment (Figure S3d) also confirms the presence of this time-dependent feature, specifically a spin-glass like behavior in the 50−80 K temperature regime. The intrinsic semiconductor property of NVOnH is demonstrated by the fit of measured electric resistivity in the region from 180 to 300 K (Figure S4). The semiconducting properties of the matrix together with the very low concentration of the magnetic moment bearing V^{4+} ions that are distributed within the nonmagnetic V^{5+} matrix represent a typical arrangement for which a spin-glass like behavior can often be observed,[36] with a variation of magnetic couplings that leads to frustration. Temperature-dependent changes of lattice parameters and geometries of magnetic coupling paths are supposed to find a special combination of values in the temperature range from 50 to 80 K that then leads supposedly to the spin-glass like behavior with the typical observed slow evolution of magnetization over time. Due to the low concentration of the magnetic ions and the low overall magnetic signal, it was not possible to further confirm a spin-glass-like behavior by ac susceptibility measurements.

For comparison, magnetic measurements were also conducted for NVO (dried NVOnH) that is obtained from NVOnH dried overnight at 300 °C under vacuum. ZFC and FC curves of NVO are also overlapping over the complete temperature region, and only the ZFC curve will be considered further. The susceptibility vs temperature curve obtained from the ZFC exhibits a clear $1/T$-like behavior typical for Langevin-type paramagnetism of localized moments. A Curie−Weiss fit (Figure 1d) gets a Curie constant of 0.1262(5) $cm^3\ K\ mol^{-1}$, a Weiss constant of −4.49(4) K, and a temperature-independent paramagnetic contribution of $7.54(6) \times 10^{-4}\ cm^3\ mol^{-1}$. Therefore, the concentrations of 1.66(1) V^{5+} and 0.34(1) V^{4+} are determined and agree well with charge neutrality conditions for the composition $Na_{0.38}V_2O_5$. This suggests that considerably more V^{4+} ions are present in NVO compared with that of NVOnH. A theoretical saturation magnetization of 0.34 μ_B per f.u. is predicted for the hypothetical free ion case. Meanwhile, the field scan at 2 K shows a typical behavior of Langevin-type localized moments and provides measured saturation magnetization of 0.123 μ_B per f.u. at 2 K and 7 T (Figure S5a), implying that some sort of anisotropies or exchange is reducing the measured ordered moment compared to the hypothetical case of 0.34 μB of the free ion. Moreover, there are no indications any more for the presence of spin-glass like behavior, which is also confirmed by the time-dependent measurement of the NVO sample (Figure S5b).

2.2. Thermal Stability and Phase Evolution of NVOnH. *In situ* high-temperature synchrotron diffraction was carried out to probe the structural evolution and thermal stability of NVOnH during heating (Figure 1e). At lower temperatures (less than 125 °C), the main reflections are attributed to bilayered NVOnH. As the temperature increased to 125 °C, the reflection at 1.10° shifts to 1.14° with a significant maximum intensity decrease, the reflection at 3.30° completely disappears, and two reflections at 4.39 and 4.59° show an intensity decrease. With the temperature increased to 150 °C, the reflection at 1.14° continuously shifts to 1.29° with a further intensity decrease, and two reflections at 2.61 and

https://doi.org/10.1021/acs.chemmater.4c01739
Chem. Mater. 2024, 36, 10176−10185

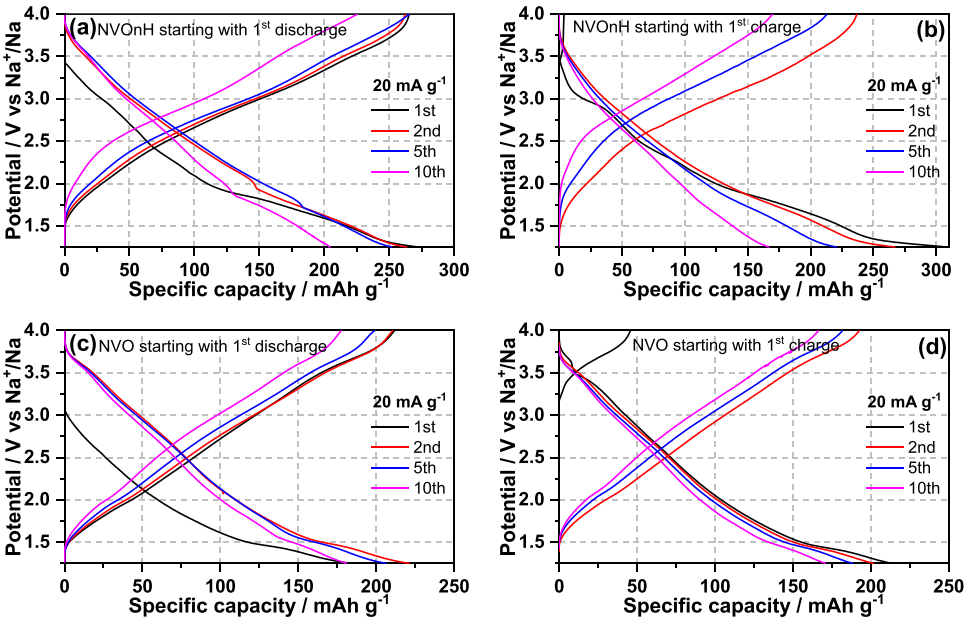

Figure 2. Charge−discharge curves of NVOnH (a, b) and NVO (c, d) starting with the first discharge and charge.

4.71° appear. With the further temperature increase to 175 °C, all reflections grow up, demonstrating a two-phase transition in the temperature range of 125−175 °C, accompanying crystal water release and O_2 release as proved by TGA-MS. In the temperature range of 175−300 °C, all reflections display no notable changes except slight shifts in their positions, which are caused by the thermal expansion during heating. At 300 °C, some very small reflections appear at 1.63, 3.52, 4.05, 4.36, 5.42, and 8.53°. Then, many other reflections such as 1.24, 1.71, 2.03, 2.23, 2.35, 2.49, 3.06, 3.25, 3.39, 3.71, 3.84, 3.98, 4.05, 4.09, and 4.35° also appear and grow as the temperature is increased to 450 °C, while all reflections of $Na_{0.38}V_2O_5$ gradually disappear. These new reflections at 450 °C correspond to two new phases 67(1) wt % of $Na_{0.33}V_2O_5$[37] ($C2/m$, a = 15.582 Å, b = 3.613 Å, c = 10.143 Å, β = 109.45°) and 33(1) wt % of $Na_{1.2}V_3O_8$[38] ($P2_1m$, a = 7.317 Å, b = 3.609 Å, c = 12.226 Å, β = 107.17°), as shown in Figure S6, indicating the decomposition of $Na_{0.38}V_2O_5$ in the temperature range of 350−450 °C. Upon further heating to 550 °C, the reflections of $Na_{0.33}V_2O_5$ slowly shift to lower angles with a slight increase in their intensities related to the thermal expansion at high temperatures. Meanwhile, the reflections of $Na_{1.2}V_3O_8$ also gradually shift to lower angles, but with a decrease in their intensities. With the further increase in temperature to 650 °C, only small changes, such as the intensity decrease of the reflection at 1.68° and the shifting to lower angles of most of the reflections, can be obtained, indicating the lattice expansion and high stability of both materials at high temperatures. Note that crystalline water is critical to expanding the spacing of the layered structure and can significantly impact the electronic structure of vanadium oxides. Meanwhile, the crystal water can also improve Na-ion diffusion in the crystal host and at the interface due to the shielding effect of the large Na^+ ions, thus affecting the electrochemical performance (capacity and rate capability).

2.3. Electrochemical Properties of NVOnH and NVO. The electrochemical properties of NVOnH and NVO were studied at 20 mA g^{-1} starting with the first discharge and charge. For NVOnH, starting with the first discharge, it displays slope-like discharge/charge profiles and delivers a first discharge/charge capacity of 273/265 mAh g^{-1}, resulting in 97% initial Coulombic efficiency (CE) (Figure 2a). NVOnH can offer a discharge capacity of 252 mAh g^{-1} for the fifth cycle, while it displays a fast capacity decay to 100 mAh g^{-1} for the 20th cycle and down to 46 mAh g^{-1} with 17% capacity retention after 100 cycles (Figure S7a). For NVOnH, starting with the first charge (Figure 2b), it shows a multiple slope profile for the first discharge and slope-like discharge/charge profiles for the rest. It delivers a first charge capacity of only 4 mAh g^{-1} and a much higher first discharge capacity of 309 mAh g^{-1}, indicating that no Na^+ ions can be extracted from the NVOnH structure. This is in good agreement with the existence of additional oxygen in the structure. It exhibits a sharp capacity decay to 94 mAh g^{-1} for the 20th cycle and down to 23 mAh g^{-1} for the 100th cycle with 7% capacity retention (Figure S7b).

In contrast, the NVO also shows slope-like discharge/charge profiles. In the case of starting with the first discharge, NVO only provides a first discharge/charge capacity of 185/212 mAh g^{-1}, resulting in 115% initial CE (Figure 2c) over 100%. This is attributed to the fact that part of Na^+ ions are extracted out from the initial $Na_{0.38}V_2O_5$ structure. It displays the highest discharge capacity of 222 mAh g^{-1} for the second cycle and a capacity fade down to 46 mAh g^{-1} for the 100th cycle with 21% capacity retention after 100 cycles (Figure S7c). For the cycling starting with the first charge (Figure 2d), it delivers a first charge capacity of 46 mAh g^{-1} (0.33−0.36 Na^+) and a first discharge capacity of 214 mAh g^{-1}, implying that almost all Na^+ ions are extracted from the NVO structure. This is in line with the result of magnetic measurements performed for NVO. It also exhibits a capacity decay to 44 mAh g^{-1} for the 100th cycle with 21% capacity retention (Figure S7d). Unfortunately, both materials undergo fast capacity fading over the initial 20 cycles. The main reason for the degradation could be attributed to the irreversibility of the materials, the (partial) dissolution of vanadium oxide, and the side reaction during cycling. It is rather complicated and challenging to understand the cause of capacity decay with cycling since it relies on many

https://doi.org/10.1021/acs.chemmater.4c01739
Chem. Mater. 2024, 36, 10176−10185

factors and the interplay of components in the cell. However, detailed investigations should be performed in future work.

2.4. Reaction Mechanism of NVOnH and NVO. To illustrate the structural evolution of NVOnH upon Na^+ (de)insertion, *in operando* synchrotron diffraction was conducted during the initial cycle, as displayed in Figure 3.

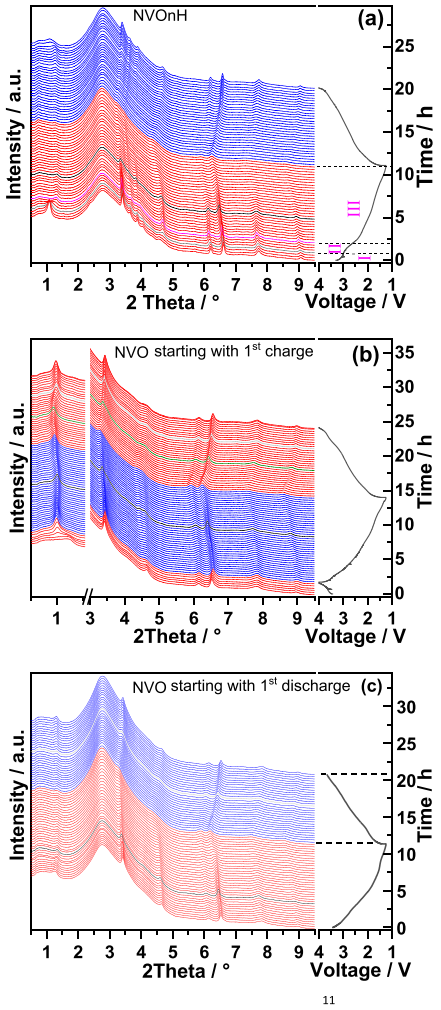

Figure 3. *In operando* synchrotron diffraction (λ = 0.20734 Å, 60 keV) of NVOnH (a), NVO starting with the first charge (b), and NVO starting with the first discharge (c) during the first cycles at 25 mA g^{-1}.

Before discharge, all reflections can be indexed according to pristine NVOnH. During the initial Na^+-ion insertion in Region I (Figure 3a), minor changes can be observed, such as the intensity decrease of the reflection at 1.09° and the slight shifts to lower angles for reflections at 3.40, 6.21, 6.61, and 7.72°, indicating a short solid-solution reaction. Upon further Na^+-ion insertion in Region II, the reflection at 1.09° significantly decreases in intensity and then disappears, accompanied by the appearance of a broad reflection at 1.30° and disappearance of reflections at 3.64, 3.88, 4.57, and 6.20°. Meanwhile, new reflections appear at 3.70, 3.96, 4.69, and 6.14° and several reflections (3.40, 6.60, 7.73, and 9.05°) move toward lower angles (3.39, 6.57, 7.67, and 9.00°, respectively). This indicates the coexistence of a two-phase transition and solid-solution process, which can probably be attributed to disordered Na^+ ions leading to a nonequilibrium condition. In Region III, notable shifts to lower angles are observed for all reflections at 3.39, 3.68, 4.69, 6.57, 6.70, 7.67, and 9.00°, while the reflection at 1.30° remains in the same position until the "black line" and then shifts to a higher angle, implying that a solid-solution reaction is present in this region. Note that all reflections slowly decrease in their intensities after the "black line" in Region III, suggesting the presence of a strong disordered structure after Na-ion insertion (Figure S8). During the charge process, it displays a reversible evolution of the diffraction pattern, and all reflections almost return back to their original positions except for the two reflections at 1.09 and 3.40° with lower intensities (Figure S8).

In the case of NVO starting with the first charge (Figure 3b), the reflection at 1.25° disappears, and a new reflection at 1.02° appears and slowly grows up, while the other reflections remain at the same positions, indicating a short two-phase transition during Na-ion deinsertion. Upon further Na-ion deinsertion (at 4.0 V), the reflection at 1.02° shifts to 0.99° (corresponding to a lattice distance of 11.9 Å), while the reflections at 3.42, 6.53, and 8.97° slightly shift toward higher angles (3.44, 6.56, and 9.00°), indicating a short solid solution to form Na-free V_2O_5. Note that the Na-free V_2O_5 does not match with any known V_2O_5 polymorphs such as α-, β-, δ-, γ-, ζ-, and ε-V_2O_5,[39] suggesting a new structure of V_2O_5. During the first discharge, all reflections except the one at 0.99° gradually move toward lower angles, while the one at 0.99° first shifts to a higher angle of 1.01° before the "black line" in Figure 3b and then shifts to a lower angle of 0.96°. This suggests that the Na-free V_2O_5 undergoes a solid-solution reaction accompanying the Na-ion insertion, where the interlayer spacing first shrinks upon the initial Na-ion insertion and then expands with enough Na-ion storage between the layers due to the strong interaction of Na ions inside the structure. During the second charge, all reflections except the one at 0.96° gradually shift back to their original positions (Figure S9), while the one at 0.96° first shifts to 0.93° before the "olive line" in Figure 3b, then shifts to a higher angle of 1.01° (light gray line), and finally returns back to 0.99°. This indicates that the material experiences a reversible but unsymmetric solid-solution reaction during the Na-ion (de)-insertion.

In the case of NVO, starting with the first discharge (Figure 3c), NVO demonstrates a completely different structural evolution compared with the described two cases. During the first discharge, all reflections except the one at 1.25° gradually move toward lower angles, while the one at 1.25° first shifts to a higher angle of 1.34° before the "black line" in Figure 3c is reached and then remains in the same position, implying that NVO only experiences a solid-solution reaction. During the first charge, all reflections show a reversible and symmetric process and finally return back to their original positions with slightly lower intensities (Figure S10), indicating the high reversibility during Na-ion insertion and deinsertion. However, the crystal structure of both NVOnH and NVO does not exhibit the same structural evolution as other vanadium oxides. For example, Muller-Bouvet et al.[40] reported that upon Na insertion, α-V_2O_5 maintained its structure without significant changes at low sodium amounts ($x \leq 0.2$ in $Na_xV_2O_5$) and experienced a solid-solution mechanism in the range $0.2 \leq x \leq 1.6$. The irreversible NaV_2O_5 phase is formed during the first Na insertion, and the NaV_2O_5 phase can reversibly insert 0.8 sodium ions in the range of 1.4−3.0 V vs Na^+/Na. Meanwhile, Ali et al.[41] proposed a different reaction mechanism: A two-

https://doi.org/10.1021/acs.chemmater.4c01739
Chem. Mater. 2024, 36, 10176−10185

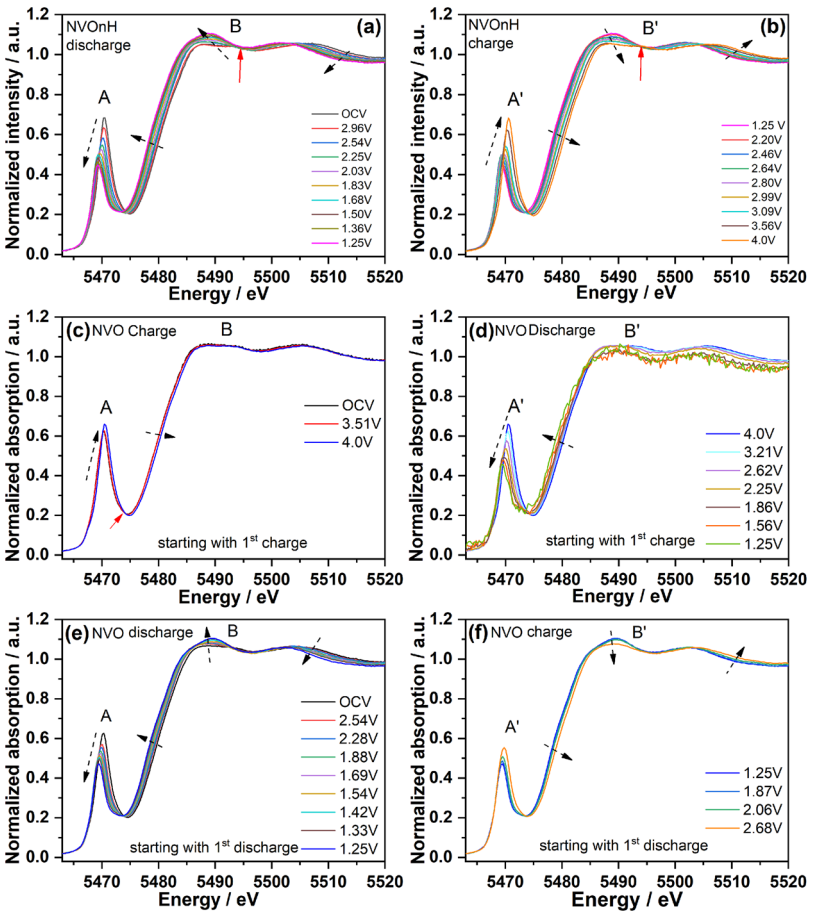

Figure 4. *In operando* V K-edge XANES spectra of NVOnH (a, b), NVO starting with the first charging (c, d), and NVO starting with the first discharging (e, f) during the first cycle; the isosbestic points are pointed out by red arrows.

phase mixture composed of a major phase of NaV_2O_5 and a minor phase of $Na_2V_2O_5$ was observed during the discharge process, where the $Na_2V_2O_5$ phase exists in the presence of crystalline and amorphous-like phases. Upon the charging process, it returns back to its original structure of V_2O_5 with a minor phase of NaV_2O_5. Baddour-Hadjean et al.[42] reported that chemically synthesized γ'-V_2O_5 experienced a two-phase mechanism in the region of $0 \leq x \leq 0.7$ (γ-$Na_{0.7}V_2O_5$) and a single-phase region in the region of $0.7 < x \leq 0.97$. Later on, they reported that ball-milled γ'-V_2O_5 demonstrated a shortening of the two-phase region and enlarged single-phase region ($0 \leq x < 0.2$ and $0.4 \leq x \leq 0.94$ in γ-$Na_xV_2O_5$).[43] Tepavcevic et al.[44] revealed that bilayered V_2O_5 underwent the expansion of layer spacing upon Na^+-ion insertion, while it lost the long-range order and maintained its short-range order after Na^+-ion deinsertion. Wei et al.[20] obtained a lattice breathing for bilayered V_2O_5 during Na^+-ion insertion and the lattice breathing can be greatly inhibited for the iron-ion preintercalated bilayered V_2O_5 via *ex situ* XRD. Dong et al.[45] claimed that NaV_6O_{15} underwent a single-phase reaction during Na^+-ion insertion/deinsertion. However, the appearance of two new reflections at 20 and 35° in the *in situ*/*operando* XRD data, accompanying the disappearance of 200 and 31−1 reflections, probably suggests the formation of a new phase. Up to now, limited *in situ* and *operando* XRD analyses of vanadium oxides for SIBs have been reported. Therefore, more efforts are needed to understand the structural evolution of vanadium oxides.

In operando XAS was conducted to look into the electronic and structural environments of V ions in NVOnH and NVO during cycling. Figure 4a displays the normalized V K-edge spectra of NVOnH during the first cycle. The oxidation state of V in NVOnH is estimated to be +4.87 using linear combination fitting (LCF) (Figure S11a), which is in good agreement with the XPS result. Moreover, an intense pre-edge peak for the V K-edge is observed owing to the 5-fold coordinated V ions by oxygens in a distorted tetragonal pyramid, which is attributed to the transitions between the 1s and bound p-hybridized d-states.[46,47] NVOnH shows a similar XAS feature to a xerogel material, suggesting a similar structure comparing NVOnH with electrolytic vanadium oxide e-V_2O_5,[27] which is also close to that of V_2O_5. Upon Na^+ insertion, the V K-edge of NVOnH and pre-peak gradually move to lower binding energies, indicating the reduction of the V oxidation state (Figure 4a). At the same time, the pre-peak exhibits a simultaneous decrease in intensity, implying the symmetry increase of local V environments. The increase in symmetry would reduce the probability of the 1s−3d transition, thus causing a reduction of the peak intensity.[48] Notable changes in both shape and intensity of edge resonance (B in Figure 4a) are observed, which is attributed to the absorption of photons accompanied by core−electron excitations.[47,49] Two small broad peaks at 5488 and 5493 eV progressively merge into one big broad peak at ∼5489 eV with a slight increase in intensity, while the peak at 5507 eV significantly moves to a lower energy of 5502 eV. A distinct

https://doi.org/10.1021/acs.chemmater.4c01739
Chem. Mater. 2024, 36, 10176−10185

isosbestic point[50] at ~5494 eV (red arrows in Figure 4a,b) can be observed for discharge and charge, respectively, suggesting a two-phase reaction[50] during Na^+ (de)insertion, as demonstrated by *in operando* synchrotron diffraction. The V oxidation state at 1.25 V is estimated as +4.0 using LCF (Figure S11b), which is close to the value from the electrochemistry (+3.84). Upon Na^+ deinsertion, the positions of the V K-edge, of the pre-edge peak, and of the edge resonance recover their initial positions. This means that the oxidation state and the local structure of the V ions behave reversibly (Figure 4b). Meanwhile, the slight difference in XAS for OCV and 4.0 V can be due to the minor Na^+ extraction from the initial structure (Figure S12).

The normalized V K-edge spectra of NVO with starting discharge and charge are shown in Figure 4c−f. Compared with that of NVOnH, the V K-edge spectrum at the OCV (Figure S13a) exhibits a slightly lower energy for its edge position and pre-peak with decreased intensity, implying the reduction of V ions as indicated by the results from magnetic measurements and electrochemistry. Moreover, only two broad peaks centered at 5489 and 5504 eV are observed, which is similar to a certain amount of Na^+-ion insertion for the pristine NVOnH. In contrast, NVO starting with the first charge displays the oxidation of V ions during the initial Na^+-ion deinsertion owing to the clear shifting toward a higher energy of the edge positions and pre-peak with a slight increase in the intensity of the pre-peak (Figure 4c). During the initial Na^+-ion insertion (Figure 4d), it also exhibits a shift to a lower energy of the edge positions and pre-peak with a gradual decrease in intensity, indicating the reduction of V ions and symmetry increase of local V environments. Interestingly, the V K-edge spectra of NVO and NVOnH at 1.25 V are close to each other, suggesting a similar oxidation state of V ions in the three cases (Figure S13b). Moreover, a distinct isosbestic point[50] at ~5474 eV (red arrow in Figure 4c) is observed and no isosbestic point (Figure 4d) is observed, implying a two-phase reaction[50] during Na^+-ion deinsertion and solid-solution reaction during the initial Na^+-ion insertion, as revealed by *in operando* synchrotron diffraction. In the case of NVO with the starting discharge (Figure 4e,f), it demonstrates a similar XAS feature evolution to NVOnH including its edge positions and pre-peak shifting toward a lower energy with a gradual decrease in the intensity of the pre-peak and edge resonance. Nevertheless, unfortunately, the data collection of the discharging process is not complete because of a beam loss during the experiment. Note that no distinct isosbestic point is obtained during the discharge and charge, implying the solid-solution reaction, in good agreement with *in operando* synchrotron diffraction.

3. CONCLUSIONS

Oxygen-rich NVOnH is successfully synthesized via a hydrothermal method, which is proven by mass spectrometry and magnetic results. The bilayered NVOnH has an orthorhombic structure and a large interlayer spacing of ~11.1 Å. NVOnH and NVO exhibit a typical Langevin-type paramagnetism of localized moments, while only NVOnH shows a spin-glass like behavior. NVOnH undergoes several notable structural evolutions and thermal instabilities during heating due to crystal water and O_2 release (125−175 °C) and decomposition of $Na_{0.38}V_2O_5$ (350−450 °C). As a cathode, NVOnH delivers a capacity of over 250 mAh g^{-1} in the initial few cycles and NVO provides a capacity of 220 mAh g^{-1}. However, both NVOnH and NVO demonstrate fast capacity decay in the first 20 cycles and low capacity retention after 100 cycles. Moreover, the reaction mechanism and reversibility of NVOnH and NVO during Na^+-ion (de)insertion are investigated via *in operando* techniques. NVOnH experiences a two-phase reaction and solid-solution reaction during discharge and charge processes, respectively, whereas NVO goes through different reaction mechanisms starting with charging and discharging. *In operando* XAS demonstrates the variation of the oxidation state and the local electron environment of V during Na^+ (de)insertion. This work provides a deep understanding of the Na^+ storage mechanism of cathode materials.

4. EXPERIMENTAL AND CALCULATIONS DETAILS

4.1. Synthesis of $Na_xV_2O_{5+\delta}\cdot nH_2O$ Nanowires. $Na_xV_2O_{5+\delta}\cdot nH_2O$ (NVOnH) nanowires were prepared via a hydrothermal method. Briefly, 0.5 g of commercial V_2O_5 powder (Alfa Aesar, 99.99%) was added to 20 mL of deionized water under vigorous stirring for 10 min to form a light orange suspension. Then, 5 mL of 30% hydrogen peroxide (H_2O_2) was dropwise added to the above suspension with stirring for 20 min to get a transparent reddish-brown solution. Afterward, a solution consisting of 0.11275 g of Na-$(CH_3COO)_2$ dissolved in 5 mL of deionized water was added into the above reddish-brown solution with stirring for 10 min. The obtained solution was transferred to a 50 mL Teflon-lined stainless-steel autoclave and kept at 200 °C for 48 h. The precipitate was washed with deionized H_2O and ethanol several times and dried at 75 °C for 12 h. The dehydrated sample NVO was prepared in a vacuum oven (Büchi Labortechnik GmbH) at 300 °C for 24 h.

4.2. Morphological and Structural Study. The morphologies were studied with a Zeiss Supra 55 Scanning Electron Microscope (SEM) with a primary energy of 15 keV. The structural characterization was performed on a STOE STADI P diffractometer operated with Mo $K_{\alpha 1}$ radiation (λ = 0.70932 Å). The powders were filled in 0.5 mm Ø borosilicate capillaries, and diffraction patterns were collected in capillary geometry. Thermogravimetric analyses (TGA) were done on an STA 449C (Netzsch GmbH) under Ar flow to determine the crystal water content in NVOnH. Simultaneous thermogravimetric analysis and mass spectrometry (TGA-MS) were conducted with a Setaram thermal analyzer SENSYS evo TGA equipped with a Pfeiffer OmniStar mass spectrometer for the analysis of the evolved gas. The measurement was conducted from room temperature to 650 °C with a heating rate of 5 °C min^{-1} under argon flow. X-ray photoelectron spectroscopy (XPS) was performed using a K-Alpha spectrometer (ThermoFisher Scientific, UK) equipped with a microfocused, monochromated Al K_α X-ray source (λ = 1486.6 eV) with a spot size of 400 μm. A charge compensation system was employed during measurement, using electrons of 8 eV energy and low-energy Ar ions to prevent localized charge accumulation. Thermo Avantage software was used in data acquisition and processing, as described elsewhere.[51] The analyzer transmission function, Scofield sensitivity factors, and effective attenuation lengths for photoelectrons were applied.[52] The standard TPP-2 M formalism was used for the calculation of effective attenuation lengths.[53] All spectra were referenced to the carbonaceous C 1s peak (C−C and C−H) at 285.0 eV binding energy.

Magnetic properties were measured by using the Vibrating Sample Magnetometry (VSM) option installed onto a DynaCool Physical Property Measurement System (PPMS) from Quantum Design. Magnetic moment vs temperature was measured at a magnetic field of 10 kOe (1 T) from 2 to 300 K with a temperature resolution of ΔT = 1 K and temperature settle mode for 2−50 K and a scan rate of 2 K/min for 50−300 K. The sample was first cooled down from RT to 2 K without a field (zero field cooling; ZFC) prior to the measurement, and then, the procedure was repeated with a field set to 1 T (field cooled; FC). The measured raw data of the temperature scans was corrected for diamagnetic contributions from the sample holder ($\chi^{dia}_{holder} = -2.5 \times 10^{-8}$ cm^3/holder) and for diamagnetic contribution

https://doi.org/10.1021/acs.chemmater.4c01739
Chem. Mater. 2024, 36, 10176−10185

from the Na^+, V^{5+}, and O^{2-} ions and from the water by the incremental method[54] ($\chi^{dia}_{closed\ shells} = -8.434 \times 10^{-5}$ cm^3 mol^{-1}). The other data sets were not corrected for diamagnetic contributions. The amount of crystal water was set to $n = 1.1$ for the calculation of molar mass and diamagnetic susceptibility.

Magnetic moment vs field (full loops) were measured at 2, 10, 20, 30, 80, 100, 150, 200, 250, and 300 K with maximum field of $\mu_0 H = 7$ T. The full loop was first measured at 2 K (with the sample cooled to 2 K in 7 T), and then, the temperature was increased to the next temperature with the field still set to 7 T to measure another loop.

Time-dependent magnetization measurements were carried out under zero field cooled from 100 K to 10, 20, 30, 40, 45, 50, 55, 60, 65, 70, 75, 80, 90, and 100 K with 10 K/min with a magnetic field of 2500 Oe for 120 min. The temperature cycling experiment was performed with a field of 1 T to trace magnetic moment during heating from 20 to 110 K and cooling again to 20 K several times at 1 K/min rate. Electric transport measurements were carried out with the ETO transport option and the Wimbush press contact assembly for PPMS (4 pins in line: I+V+V−I-; pin-pin distance 2 mm). Four-wire measurements were performed using a pellet of 8 mm diameter from 180 to 200 K ($\Delta T = 2$ K) and 10^{-4} mA ac-excitation and from 210 to 300 K ($\Delta T = 10$ K) and 10^{-5} mA ac-excitation (both with 0.5 Hz). However, the four-wire measurement is not possible anymore at temperatures below 180 K due to the high resistivity over 10 MOhm. Data were collected with 5 s averaging time each per temperature.

In situ high-temperature synchrotron diffraction was performed at beamline P02.1, PETRA-III at DESY in Hamburg, Germany, using synchrotron radiation $\lambda = 0.20734$ Å (60 keV). The quartz capillary filled with NVOnH powder was heated in a Hot Air Blower, Oxford (RT to 1200 K) oven under Ar from room temperature to 650 °C with a ramp of 50 K/min. DAWN software is used to process the 2D powder diffraction.[55]

4.3. Electrochemical Characterizations. The electrode was prepared by coating a slurry mixture on a stainless steel foil (SS) or Al foil, consisting of an active material (NVOnH using SS foil or NVO using Al foil), C65 (Timcal), and a polyvinylidene difluoride (PVDF) binder in a mass ratio of 70:20:10 using an *N*-methyl-2-pyrrolidone solvent. The electrode (mass loading of 1.6−2.3 mg cm^{-2}) was dried at 65 °C overnight and then cut into discs of 12 mm diameter and then dried again under vacuum at 65 °C overnight before being put into a glovebox. The electrochemical performance of the cathode materials was investigated in 2032-coin cells, where metallic sodium was used as a counter electrode with a Whatman glass fiber separator. The electrolyte was 1 M $NaClO_4$ in a mixture of ethylene carbonate (EC):propylene carbonate (PC) (1:1 by volume) and 5% fluoro-ethylene carbonate (FEC). Galvanostatic cycling with potential limitation (GCPL) and cyclic voltammetry (CV) measurements were conducted in a working potential of 1.25−4.0 V vs Na^+/Na on a VMP3 potentiostat (BioLogic) at 25 °C.

4.4. *In Operando* Synchrotron Diffraction and *In Operando* X-ray Absorption Spectroscopy (XAS). *In operando* synchrotron diffraction was performed at the Material Science and Powder Diffraction beamline (MSPD) at ALBA, Spain and at PETRA-III beamline P02.1 at DESY in Hamburg, Germany. The electrochemical cells consist of 2025-type coin cell with glass windows of 5 mm diameter for beam entrance. The positive electrode (active materials, 2 mg, and ∼7 mg cm^{-2}) was prepared by pressing the electrode mixture on Al mesh within a 5 mm hole in the center.

In operando synchrotron diffraction was conducted at ALBA with radiation $\lambda = 0.4131$ Å wavelength (30 keV) and position sensitive detector MYTHEN, where preliminary data were collected with an effective exposure time of 60 s in steps of 0.006° during the first cycles at 20 mA g^{-1}. *In operando* synchrotron diffraction was conducted at DESY with radiation $\lambda = 0.20734$ Å wavelength (60 keV), where data were collected with an effective exposure time of 40 s during the first cycles at 25 mA g^{-1}. DAWN software was used for the integration of the 2D images collected with Varex XRD 4343CT detector (150 × 150 μm^2 pixel size, 2880 × 2880 pixel area) into 1D pattern. Powder of LaB_6 standard (NIST SRM6 60c) was used for the detector calibration.[55] The diffraction data analysis was carried out by the Rietveld method using the Fullprof software package.[56] *In operando* XAS measurements were performed at synchrotron beamline P65 at PETRA III (DESY, Hamburg).[57] XAS was conducted during the first cycle at a current of 25 mA g^{-1} in the same coin cell configuration with a Kapton window. XAS spectra at the V K-edge were recorded in quick-XAS (6 min/spectrum) mode in fluorescence geometry using PIPS (passivated implanted planar silicon) diode detector. The monochromator was calibrated using a vanadium foil and V K-edge spectra for NVOnH and NVO. V_2O_3, VO_2, and V_2O_5 were used as the standard materials. All data were collected at room temperature with a double crystal monochromator of Si(111) crystal, and all XAS spectra were processed using the DEMETER software package.[58]

■ ASSOCIATED CONTENT

Data Availability Statement

The original data are available at KITOpen through the DOI: 10.35097/ejazcks3bd5v3fq2.

Supporting Information

The Supporting Information is available free of charge at https://pubs.acs.org/doi/10.1021/acs.chemmater.4c01739.

SEM, TGA, XPS, magnetic measurements, resistivity of pristine NVOnH; magnetic measurements of NVO; Rietveld refinement; Cycling performance of NVOnH and NVO; XRD of NVOnH and NVO at different charged states; LCF of the derivative V K-edge XANES spectrum of NVOnH; V K-edge XANES spectra of NVOnH and NVO; (Figure S1−13) (PDF)

■ AUTHOR INFORMATION

Corresponding Author

Qiang Fu − *Institute for Applied Materials (IAM), Karlsruhe Institute of Technology (KIT), Karlsruhe D-76344, Germany;* orcid.org/0000-0002-2507-5477; Phone: 49-721 608-41445; Email: qiang.fu@kit.edu; Fax: 49-721 608-28521

Authors

Björn Schwarz − *Institute for Applied Materials (IAM), Karlsruhe Institute of Technology (KIT), Karlsruhe D-76344, Germany;* orcid.org/0000-0002-9461-1448

Angelina Sarapulova − *Institute for Applied Materials (IAM), Karlsruhe Institute of Technology (KIT), Karlsruhe D-76344, Germany;* orcid.org/0000-0003-4643-3912

Xianlin Luo − *Institute for Applied Materials (IAM), Karlsruhe Institute of Technology (KIT), Karlsruhe D-76344, Germany*

Julian Hansen − *Institute for Applied Materials (IAM), Karlsruhe Institute of Technology (KIT), Karlsruhe D-76344, Germany*

Zhen Meng − *Helmholtz Institute Ulm for Electrochemical Energy Storage (HIU), Ulm 89081, Germany;* orcid.org/0000-0001-5756-9159

Volodymyr Baran − *Deutsches Elektronen-Synchrotron (DESY), Hamburg 22607, Germany;* orcid.org/0000-0003-2379-3632

Alexander Missyul − *CELLS-ALBA Synchrotron, Barcelona E-08290, Spain;* orcid.org/0000-0002-0577-4481

Edmund Welter − *Deutsches Elektronen-Synchrotron (DESY), Hamburg 22607, Germany*

Weibo Hua − *Institute for Applied Materials (IAM), Karlsruhe Institute of Technology (KIT), Karlsruhe D-76344, Germany; School of Chemical Engineering and*

https://doi.org/10.1021/acs.chemmater.4c01739
Chem. Mater. 2024, 36, 10176−10185

Technology, Xi'an Jiaotong University, Xi'an, Shaanxi 710049, China; orcid.org/0000-0001-5372-4422
Michael Knapp − *Institute for Applied Materials (IAM), Karlsruhe Institute of Technology (KIT), Karlsruhe D-76344, Germany;* orcid.org/0000-0003-0091-8463
Helmut Ehrenberg − *Institute for Applied Materials (IAM), Karlsruhe Institute of Technology (KIT), Karlsruhe D-76344, Germany;* orcid.org/0000-0002-5134-7130
Sonia Dsoke − *Institute for Applied Materials (IAM), Karlsruhe Institute of Technology (KIT), Karlsruhe D-76344, Germany;* orcid.org/0000-0001-9295-2110

Complete contact information is available at: https://pubs.acs.org/10.1021/acs.chemmater.4c01739

Notes

The authors declare no competing financial interest.

■ ACKNOWLEDGMENTS

This work contributes to the research performed at CELEST (Center for Electrochemical Energy Storage Ulm-Karlsruhe) and was funded by the German Research Foundation (DFG) under Project ID 390874152 (POLiS Cluster of Excellence). Our research work has gained benefit from beamtime allocation (2020024277-qfu) at BL04 - MSPD at ALBA Synchrotron, Barcelona, Spain. We acknowledge DESY (Hamburg, Germany), a member of the Helmholtz Association HGF, for the provision of experimental facilities. Parts of this research were carried out at PETRA III beamlines P02.1, P64 and P65. Beamtime was allocated for proposal(s) beamline P02.1 (I-20211294, I-20210724), P64 (I-20210715) and P65 (I-20211296). The *in operando* XAS work was performed by using the Biologic potentiostat of PETRA-III beamline P02.1. We thank Francois Fauth from Experiments Division at ALBA for his technical help during synchrotron diffraction measurement. Thomas Bergfeldt (IAM-AWP), Bettina Hunzinger, and Liuda Mereacre are gratefully acknowledged for ICP-OES, SEM, and TGA measurements, respectively.

■ REFERENCES

(1) Hamon, Y.; Brousse, T.; Jousse, F.; Topart, P.; Buvat, P.; Schleich, D. M. Aluminum Negative Electrode in Lithium Ion Batteries. *J. Power Sources* **2001**, *97*−*98*, 185−187.
(2) Obrovac, M. N.; Chevrier, V. L. Alloy Negative Electrodes for Li-Ion Batteries. *Chem. Rev.* **2014**, *114*, 11444−11502.
(3) Jian, Z.; Yuan, C.; Han, W.; Lu, X.; Gu, L.; Xi, X.; Hu, Y.-S.; Li, H.; Chen, W.; Chen, D.; Ikuhara, Y.; Chen, L. Atomic Structure and Kinetics of NASICON $Na_xV_2(PO_4)_3$ Cathode for Sodium-Ion Batteries. *Adv. Funct. Mater.* **2014**, *24*, 4265−4272.
(4) Zhang, H.; Tan, X.; Li, H.; Passerini, S.; Huang, W. Assessment and Progress of Polyanionic Cathodes in Aqueous Sodium Batteries. *Energy Environ. Sci.* **2021**, *14*, 5788−5800.
(5) Yabuuchi, N.; Kubota, K.; Dahbi, M.; Komaba, S. Research Development on Sodium-Ion Batteries. *Chem. Rev.* **2014**, *114*, 11636−11682.
(6) Hwang, J.-Y.; Myung, S.-T.; Sun, Y.-K. Sodium-Ion Batteries: Present and Future. *Chem. Soc. Rev.* **2017**, *46*, 3529−3614.
(7) Jia, X. B.; Wang, J.; Liu, Y. F.; Zhu, Y. F.; Li, J. Y.; Li, Y. J.; Chou, S. L.; Xiao, Y. Facilitating Layered Oxide Cathodes Based on Orbital Hybridization for Sodium-Ion Batteries: Marvelous Air Stability, Controllable High Voltage, and Anion Redox Chemistry. *Adv. Mater.* **2024**, *36*, 2307938.
(8) Li, J.; Hu, H.; Wang, J.; Xiao, Y. Surface Chemistry Engineering of Layered Oxide Cathodes for Sodium-Ion Batteries. *Carbon Neutralization* **2022**, *1*, 96−116.
(9) Wang, J.; Zhu, Y.-F.; Su, Y.; Guo, J.-X.; Chen, S.; Liu, H.-K.; Dou, S.-X.; Chou, S.-L.; Xiao, Y. Routes to High-Performance Layered Oxide Cathodes for Sodium-Ion Batteries. *Chem. Soc. Rev.* **2024**, *53*, 4230−4301.
(10) Kim, H.; Kim, H.; Ding, Z.; Lee, M. H.; Lim, K.; Yoon, G.; Kang, K. Recent Progress in Electrode Materials for Sodium-Ion Batteries. *Adv. Energy Mater.* **2016**, *6*, 1600943.
(11) Xiang, X. D.; Zhang, K.; Chen, J. Recent Advances and Prospects of Cathode Materials for Sodium-Ion Batteries. *Adv. Mater.* **2015**, *27*, 5343−5364.
(12) CATL*CATL Unveils Its Latest Breakthrough Technology by Releasing Its First Generation of Sodium-ion Batteries*; 2021−07−29. https://www.catl.com/en/news/665.html.
(13) Kubota, K.; Dahbi, M.; Hosaka, T.; Kumakura, S.; Komaba, S. Towards K-Ion and Na-Ion Batteries as "Beyond Li-Ion". *Chem. Rec.* **2018**, *18*, 459−479.
(14) Yao, J.; Li, Y.; Massé, R. C.; Uchaker, E.; Cao, G. Revitalized Interest in Vanadium Pentoxide as Cathode Material for Lithium-Ion Batteries and Beyond. *Energy Storage Mater.* **2018**, *11*, 205−259.
(15) Mao, M.; Gao, T.; Hou, S.; Wang, C. A Critical Review of Cathodes for Rechargeable Mg Batteries. *Chem. Soc. Rev.* **2018**, *47*, 8804−8841.
(16) Selvakumaran, D.; Pan, A.; Liang, S.; Cao, G. A Review on Recent Developments and Challenges of Cathode Materials for Rechargeable Aqueous Zn-ion Batteries. *J. Mater. Chem. A* **2019**, *7*, 18209−18236.
(17) Moretti, A.; Passerini, S. Bilayered Nanostructured $V_2O_5{\cdot}nH_2O$ for Metal Batteries. *Adv. Energy Mater.* **2016**, *6*, 1600868.
(18) Petkov, V.; Trikalitis, P. N.; Bozin, E. S.; Billinge, S. J. L.; Vogt, T.; Kanatzidis, M. G. Structure of $V_2O_5{\cdot}nH_2O$ Xerogel Solved by the Atomic Pair Distribution Function Technique. *J. Am. Chem. Soc.* **2002**, *124*, 10157−10162.
(19) Clites, M.; Pomerantseva, E. Bilayered Vanadium Oxides by Chemical Pre-Intercalation of Alkali and Alkali-Earth Ions as Battery Electrodes. *Energy Storage Mater.* **2018**, *11*, 30−37.
(20) Wei, Q.; Jiang, Z.; Tan, S.; Li, Q.; Huang, L.; Yan, M.; Zhou, L.; An, Q.; Mai, L. Lattice Breathing Inhibited Layered Vanadium Oxide Ultrathin Nanobelts for Enhanced Sodium Storage. *ACS Appl. Mater. Interfaces* **2015**, *7*, 18211−18217.
(21) Clites, M.; Byles, B. W.; Pomerantseva, E. Effect of Aging and Hydrothermal Treatment on Electrochemical Performance of Chemically Pre-Intercalated Na-V-O Nanowires for Na-ion Batteries. *J. Mater. Chem. A* **2016**, *4*, 7754−7761.
(22) Feng, J.; Xiong, Z.; Zhao, L.; Huang, C.; Liu, H.; Chen, S.; Wang, Z.; Kuang, Q.; Dong, Y.; Fan, Q.; Zhao, Y. One-Pot Hydrothermal Synthesis of $Na_xV_2O_5{\cdot}nH_2O$/KB Nanocomposite as a Sodium-Ion Battery Cathode for Improved Reversible Capacity and Rate Performance. *J. Power Sources* **2018**, *396*, 230−237.
(23) Baddour-Hadjean, R.; Thanh Nguyen Huynh, L.; Batyrbekuly, D.; Bach, S.; Pereira-Ramos, J. P. Bilayered Potassium Vanadate $K_{0.5}V_2O_5$ as Superior Cathode Material for Na-Ion Batteries. *ChemSusChem* **2019**, *12*, 5192−5198.
(24) Durupthy, O.; Steunou, N.; Coradin, T.; Maquet, J.; Bonhomme, C.; Livage, J. Influence of pH and Ionic Strength on Vanadium(v) Oxides Formation. From $V_2O_5{\cdot}nH_2O$ Gels to Crystalline $NaV_3O_8{\cdot}1.5H_2O$. *J. Mater. Chem.* **2005**, *15*, 1090−1098.
(25) Lee, C.-Y.; Marschilok, A. C.; Subramanian, A.; Takeuchi, K. J.; Takeuchi, E. S. Synthesis and Characterization of Sodium Vanadium Oxide Gels: the Effects of Water (n) and Sodium (x) Content on the Electrochemistry of $Na_xV_2O_5{\cdot}nH_2O$. *Phys. Chem. Chem. Phys.* **2011**, *13*, 18047−18054.
(26) Zhou, W.; Chen, J.; He, C.; Chen, M.; Xu, X.; Tian, Q.; Xu, J.; Wong, C.-P. Hybridizing δ-type $Na_xV_2O_5{\cdot}nH_2O$ with Graphene towards High-Performance Aqueous Zinc-Ion Batteries. *Electrochim. Acta* **2019**, *321*, No. 134689.
(27) Potiron, E.; Le Gal La Salle, A.; Verbaere, A.; Piffard, Y.; Guyomard, D. Electrochemically Synthesized Vanadium Oxides as Lithium Insertion Hosts. *Electrochim. Acta* **1999**, *45*, 197−214.

(28) Potiron, E.; Le Gal La Salle, A.; Verbaere, A.; Piffard, Y.; Guyomard, D.; Tournoux, M. Electrochemical Synthesis, Characterization and Lithium Intercalation Properties of e-$M_xV_2O_{5+y}\cdot nH_2O$ (M = Ni^{II}, Cu^{II} or Mn^{IV}). *J. Phys. Chem. Solids* **2001**, *62*, 1447−1455.
(29) Kundu, D.; Adams, B. D.; Duffort, V.; Vajargah, S. H.; Nazar, L. F. A High-Capacity and Long-Life Aqueous Rechargeable Zinc Battery Using a Metal Oxide Intercalation Cathode. *Nat. Energy* **2016**, *1*, 16119.
(30) Andrews, J. L.; Mukherjee, A.; Yoo, H. D.; Parija, A.; Marley, P. M.; Fakra, S.; Prendergast, D.; Cabana, J.; Klie, R. F.; Banerjee, S. Reversible Mg-Ion Insertion in a Metastable One-Dimensional Polymorph of V_2O_5. *Chem.* **2018**, *4*, 564−585.
(31) Esparcia, E. A.; Chae, M. S.; Ocon, J. D.; Hong, S.-T. Ammonium Vanadium Bronze ($NH_4V_4O_{10}$) as a High-Capacity Cathode Material for Nonaqueous Magnesium-Ion Batteries. *Chem. Mater.* **2018**, *30*, 3690−3696.
(32) Wang, H.; Bi, X.; Bai, Y.; Wu, C.; Gu, S.; Chen, S.; Wu, F.; Amine, K.; Lu, J. Open-Structured $V_2O_5\cdot nH_2O$ Nanoflakes as Highly Reversible Cathode Material for Monovalent and Multivalent Intercalation Batteries. *Adv. Energy Mater.* **2017**, *7*, 1602720.
(33) Zhao, H.; Fu, Q.; Yang, D.; Sarapulova, A.; Pang, Q.; Meng, Y.; Wei, L.; Ehrenberg, H.; Wei, Y.; Wang, C. In Operando Synchrotron Studies of NH_4^+ Pre-Intercalated $V_2O_5\cdot nH_2O$ Nanobelts as the Cathode Material for Aqueous Rechargeable Zinc Batteries. *ACS Nano* **2020**, *14*, 11809−11820.
(34) Enjalbert, R.; Galy, J. A Refinement of the Structure of V_2O_5. *Acta Cryst. C* **1986**, *42*, 1467−1469.
(35) Silversmit, G.; Depla, D.; Poelman, H.; Marin, G. B.; De Gryse, R. Determination of the V2p XPS Binding Energies for Different Vanadium Oxidation States (V^{5+} to V^{0+}). *J. Electron Spectrosc. Relat. Phenom.* **2004**, *135*, 167−175.
(36) Mydosh, J. A.*Spin Glasses: An Experimental Introduction*1st Edition ed.; CRC Press: 1993.
(37) Grzechnik, A.; Ueda, Y.; Yamauchi, T.; Hanfland, M.; Hering, P.; Potapkin, V.; Friese, K. Pressure-Induced Non-Superconducting Phase of β-$Na_{0.33}V_2O_5$ and the Mechanism of High-Pressure Phase Transitions in β-$Na_{0.33}V_2O_5$ and β-$Li_{0.33}V_2O_5$ at Room Temperature. *J. Phys.: Condens. Matter* **2016**, *28*, No. 035401.
(38) Schindler, M.; Hawthorne, F. C.; Alexander, M. A.; Kutluoglu, R. A.; Mandaliev, P.; Halden, N. M.; Mitchell, R. H. Na−Li−$[V_3O_8]$ Insertion Electrodes: Structures and Diffusion Pathways. *J. Solid State Chem.* **2006**, *179*, 2616−2628.
(39) Fu, Q.; Zhao, H.; Sarapulova, A.; Dsoke, S. V_2O_5 as a Versatile Electrode Material for Post-Lithium Energy Storage Systems. *Appl. Res.* **2022**, *2*, No. e202200070.
(40) Muller-Bouvet, D.; Baddour-Hadjean, R.; Tanabe, M.; Huynh, L. T. N.; Le, M. L. P.; Pereira-Ramos, J. P. Electrochemically Formed α'-NaV_2O_5: A New Sodium Intercalation Compound. *Electrochim. Acta* **2015**, *176*, 586−593.
(41) Ali, G.; Lee, J. H.; Oh, S. H.; Cho, B. W.; Nam, K.-W.; Chung, K. Y. Investigation of the Na Intercalation Mechanism into Nanosized V_2O_5/C Composite Cathode Material for Na-Ion Batteries. *ACS Appl. Mater. Interfaces* **2016**, *8*, 6032−6039.
(42) Safrany Renard, M.; Emery, N.; Baddour-Hadjean, R.; Pereira-Ramos, J.-P. γ'-V_2O_5: A New High Voltage Cathode Material for Sodium-Ion Battery. *Electrochim. Acta* **2017**, *252*, 4−11.
(43) Baddour-Hadjean, R.; Safrany Renard, M.; Pereira-Ramos, J.-P. Enhanced Electrochemical Properties of Ball-Milled γ'-V_2O_5 as Cathode Material for Na-Ion Batteries: A Structural and Kinetic Investigation. *J. Power Sources* **2021**, *482*, No. 229017.
(44) Tepavcevic, S.; Xiong, H.; Stamenkovic, V. R.; Zuo, X. B.; Balasubramanian, M.; Prakapenka, V. B.; Johnson, C. S.; Rajh, T. Nanostructured Bilayered Vanadium Oxide Electrodes for Rechargeable Sodium-Ion Batteries. *ACS Nano* **2012**, *6*, 530−538.
(45) Dong, Y.; Xu, J.; Chen, M.; Guo, Y.; Zhou, G.; Li, N.; Zhou, S.; Wong, C.-P. Self-Assembled NaV_6O_{15} Flower-Like Microstructures for High-Capacity and Long-Life Sodium-Ion Battery Cathode. *Nano Energy* **2020**, *68*, No. 104357.
(46) Tanaka, T.; Yamashita, H.; Tsuchitani, R.; Funabiki, T.; Yoshida, S. X-Ray Absorption (EXAFS/XANES) Study of Supported Vanadium Oxide Catalysts. Structure of Surface Vanadium Oxide Species on Silica and [gamma]-Alumina at a Low Level of Vanadium Loading. *J. Chem. Soc. Faraday Transact. 1: Phys. Chem. Condens. Phase* **1988**, *84*, 2987−2999.
(47) Wong, J.; Lytle, F. W.; Messmer, R. P.; Maylotte, D. H. K-Edge Absorption Spectra of Selected Vanadium Compounds. *Phys. Rev. B* **1984**, *30*, 5596−5610.
(48) Passerini, S.; Smyrl, H. W.; Berrettoni, M.; Tossici, R.; Rosolen, M.; Marassi, R.; Decker, F. XAS and Electrochemical Characterization of Lithium Intercalated V_2O_5 Xerogels. *Solid State Ion.* **1996**, *90*, 5−14.
(49) Yoo, H. D.; Liang, Y.; Dong, H.; Lin, J.; Wang, H.; Liu, Y.; Ma, L.; Wu, T.; Li, Y.; Ru, Q.; Jing, Y.; An, Q.; Zhou, W.; Guo, J.; Lu, J.; Pantelides, S. T.; Qian, X.; Yao, Y. Fast Kinetics of Magnesium Monochloride Cations in Interlayer-Expanded Titanium Disulfide for Magnesium Rechargeable Batteries. *Nat. Commun.* **2017**, *8*, 339.
(50) Liu, X.; Wang, D.; Liu, G.; Srinivasan, V.; Liu, Z.; Hussain, Z.; Yang, W. Distinct Charge Dynamics in Battery Electrodes Revealed by In Situ and Operando Soft X-Ray Spectroscopy. *Nat. Commun.* **2013**, *4*, 2568.
(51) Parry, K. L.; Shard, A. G.; Short, R. D.; White, R. G.; Whittle, J. D.; Wright, A. ARXPS Characterisation of Plasma Polymerised Surface Chemical Gradients. *Surf. Interface Anal.* **2006**, *38*, 1497−1504.
(52) Scofield, J. H. Hartree-Slater Subshell Photoionization Cross-Sections at 1254 and 1487 eV. *J. Electron Spectrosc. Relat. Phenom.* **1976**, *8*, 129−137.
(53) Tanuma, S.; Powell, C. J.; Penn, D. R. Calculations of Electron Inelastic Mean Free Paths. IX. Data for 41 Elemental Solids Over the 50 eV to 30 keV Range. *Surf. Interface Anal.* **2011**, *43*, 689−713.
(54) Lueken, H.Einheiten, Konstanten, Inkremente. In *Magnetochemie: Eine Einführung in Theorie und Anwendung*; Vieweg+Teubner Verlag: Wiesbaden, 1999; pp 421−427.
(55) Filik, J.; Ashton, A. W.; Chang, P. C. Y.; Chater, P. A.; Day, S. J.; Drakopoulos, M.; Gerring, M. W.; Hart, M. L.; Magdysyuk, O. V.; Michalik, S. Processing Two-Dimensional X-Ray Diffraction and Small-Angle Scattering Data in DAWN 2. *J. Appl. Crystallogr.* **2017**, *50*, 959−966.
(56) Rodríguez-Carvajal, J. Recent Developments of the Program FULLPROF, in Commission on Powder Diffraction (IUCr). *Newsletter* **2001**, *26*, 12−19.
(57) Welter, E.; Chernikov, R.; Herrmann, M.; Nemausat, R. A Beamline for Bulk Sample X-Ray Absorption Spectroscopy at the High Brilliance Storage Ring PETRA III. *AIP Conf. Proc.* **2019**, *2054*, No. 040002.
(58) Ravel, B.; Newville, M. ATHENA, ARTEMIS, HEPHAESTUS: Data Analysis for X-Ray Absorption Spectroscopy Using IFEFFIT. *J. Synchrotron Radiat.* **2005**, *12*, 537−541.

https://doi.org/10.1021/acs.chemmater.4c01739
Chem. Mater. 2024, 36, 10176−10185